Science Advances

AAAS

advances.sciencemag.org/cgi/content/full/1/9/e1500701/DC1

Supplementary Materials for

Epidermal devices for noninvasive, precise, and continuous mapping of macrovascular and microvascular blood flow

R. Chad Webb, Yinji Ma, Siddharth Krishnan, Yuhang Li, Stephen Yoon, Xiaogang Guo, Xue Feng, Yan Shi, Miles Seidel, Nam Heon Cho, Jonas Kurniawan, James Ahad, Niral Sheth, Joseph Kim, James G. Taylor VI, Tom Darlington, Ken Chang, Weizhong Huang, Joshua Ayers, Alexander Gruebele, Rafal M. Pielak, Marvin J. Slepian, Yonggang Huang, Alexander M. Gorbach, John A. Rogers

Published 30 October 2015, *Sci. Adv.* **1**, e1500701 (2015)
DOI: 10.1126/sciadv.1500701

This PDF file includes:

Other Supplementary Material for this manuscript includes the following:
(available at advances.sciencemag.org/cgi/content/full/1/9/e1500701/DC1)

Movie S1A (.mp4 format). Movie of device signals over time for experiments presented in Fig. 3 (A to C).
Movie S1B (.mp4 format). Infrared movie showing the sequential pressure applications for experiments presented in Fig. 3 (A to C) and movie S1A.
Movie S2 (.mp4 format). Movie of device signals over time for experiments presented in Fig. 4 (A to D).
Movie S3 (.mp4 format). Movie of device signals over time for experiments presented in Fig. 5 (A to I).
Movie S4 (.mp4 format). Infrared movie of thermal distribution over time due to device heating for experiments presented in Fig. 5 (J to M). An arrow in the infrared movie shows the location of the pulses, which appear during the period of 460 s < t < 620 s. Text indicators are also displayed during the movie to coincide with each pulse.

Supplementary Methods: Device Fabrication

Prepare polymer base layers

1. Clean a 3” Si wafer (Acetone, IPA -> Dry 5 min at 110 °C).

2. Spin coat with PMMA (poly(methyl methacrylate) 495 A6 (Microchem), spun at 3,000 rpm for 30 s.

3. Anneal at 180 °C for 2 min.

4. Spin coat with polyimide (PI, poly(pyromellitic dianhydride-co-4,4′ -oxydianiline), amic acid solution, Sigma-Aldrich, spun at 4,000 rpm for 30 s).

5. Anneal at 110 °C for 30 s.

6. Anneal at 150 °C for 5 min.

7. Anneal at 250 °C under vacuum for 1 hr.

Deposit first metallization

8. Deposit 6/100 nm Cr/Au via electron beam evaporation.

9. Pattern photoresist (PR; Clariant AZ5214, 3000 rpm, 30s) with 365 nm optical lithography through iron oxide mask (Karl Suss MJB3).

Develop in aqueous base developer (MIF 327).

10. Etch Au with TFA Au etchant (Transene).

11. Etch Cr with CR-7 Cr Mask Etchant (Cyantek).

12. Remove PR with AZ 400-T Stripper.

13. Dry 5 min at 150 °C.

Deposit second metallization

14. Deposit 10/550/20/25 nm Ti/Cu/Ti/Au via electron beam evaporation.

15. Pattern PR AZ5214.

16. Etch Au with TFA Au etchant.

17. Etch Ti with 6:1 Buffered Oxide Etchant.

18. Etch Cu with CE-100 etchant (Transene).

19. Etch Ti with 6:1 Buffered Oxide Etchant.

20. Remove PR w/ Acetone, IPA rinse.

21. Dry 5 min at 150 °C.

Isolate entire device

22. Spin coat with PI spun at 4,000 rpm for 30 s.

23. Anneal at 110 °C for 30 s.

24. Anneal at 150 °C for 5 min.

25. Anneal at 250 °C under vacuum for 1 hr.

26. Pattern photoresist (PR; Clariant AZ4620, 3000 rpm, 30s) with 365 nm optical lithography through iron oxide mask (Karl Suss MJB3).

Develop in aqueous base developer (AZ 400K diluted 1:3, AZ 400K:Water).

27. Reactive ion *etch (50 mTorr, 80 sccm O2, 200 W, 30 min).*

Release and transfer

28. Release device by immersing in hot Acetone (60 °C) for 5 min.

29. Remove device with water-soluble tape (Wave Solder Tape, 5414, 3M).

30. Deposit 3/30 nm Ti/SiO2 onto device on water soluble tape, via electron beam evaporation.

31. Expose a ~10 μm silicone sheet (Ecoflex, Smooth-on Co.), coated on silanized glass slide, with broadband UV light for 5 min.

32. Apply water soluble tape with device to exposed silicone sheet.

33. Immerse in warm water to dissolve tape.

34. Immerse quickly in Chrome Mask Etchant to remove any remaining residue.

35. Bond thin, flexible cable (Elform, HST-9805-210) using hot iron with firm pressure.

36. Apply additional silicone (10-100 um) by doctor blade

37. Apply silicone medical tape frame (Ease Release Tape, 3M) (optional – for robust, repeated applications with a single device).

38. Remove device from glass slide.

Supplementary Materials: Peel Strength and Adhesion

Prior work from our group has demonstrated the peel strength of the silicone/skin interface to be 0.2 N/m (*26*, *29*). In the case of a device with no added support from (i.e. silicone backing only, no supporting medical tape), the overall weight of the device is 0.015 g spread over ~4 cm2, assuming 40 μm thick silicone. If, for example, the entire mass of the device were concentrated to an edge of the device under 1 G of acceleration (9.8 m/s), a peel force of .008 N/m would develop, which is 1/25 of the peel strength. The realities of imperfections in surface adhesion, combined with the fact that the entire device mass is not concentrated, lead us to consider 10s of Gs of acceleration as a general number required for delamination due to accelerations in body motion. The addition of the medical tape frame, as discussed for devices designed for repeated applications, increases the overall peel strength to 9.5 N/m +/- 2.5 N/m and the overall device weight to 0.8 g. A similar analysis as that for the no frame case results in 60 Gs of acceleration to remove the device via accelerations in body motion. Vigorous sweating has been shown to reduce the peel strength.

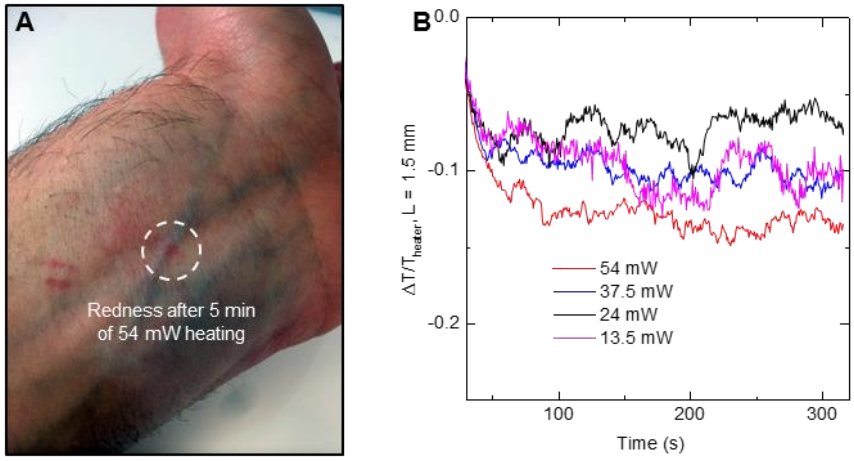

Fig. S1. Analysis of thermal actuator power levels. (**A**) Photograph of local redness (image levels enhanced for contrast) induced by 5 min of heating at 54 mW power (15.8 °C rise) to the thermal actuator. Power levels are kept below 25 mW in all experiments to avoid this type of issue. (**B**) Measured temperature differentials, taken over a vein on the wrist, for 4 different power levels. For a constant flow rate, the curves should be independent of power. However, changing flow rate in the vein can be seen by oscillations in the data. Within oscillations, the curves are independent of power until 54 mW, where the signal strength appears slightly amplified, possibly due the skin changes apparent in (A).

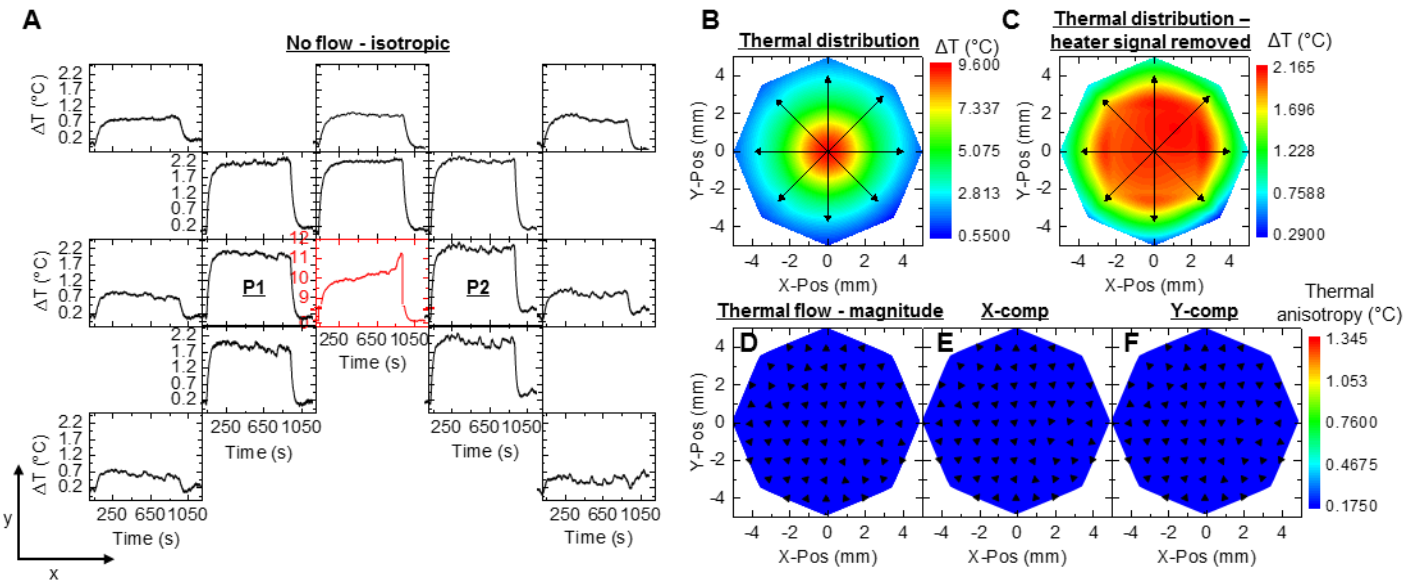

Fig. S2. Epidermal device data output for skin locations with isotropic thermal transport. Similar datasets as shown in Figure 1(D-I), except with the device placed on the palm, away from any large blood vessels.

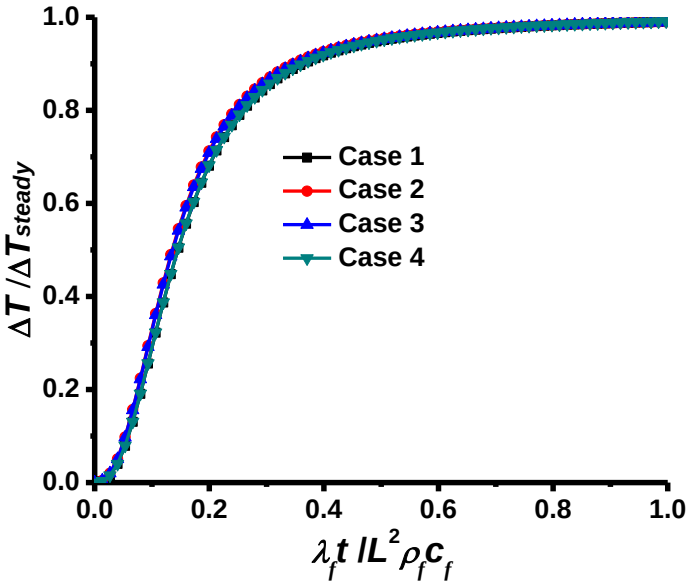

Fig. S3. FEA verification for the transient scaling law. Case 1 is the base line for comparison (water: λ_f=0.6W·mm^{-1}K^{-1}, ρ_f=1000kg/m^3, c_f=4184J·kg^{-1}·K^{-1} , PDMS: λ_s=0.18W·mm^{-1}K^{-1}, ρ_s=970kg/m^3, c_s=1380J·kg^{-1}·K^{-1} , h=0.55mm, L=1.5mm, B=1.5mm, R=1mm, v=5mm/s). Case 2 gives double the flow velocity. Case 3 changes the material properties (double λ_f and λ_s, quadruple ρ_f and ρ_s) while Case 4 varies the geometric parameters (double h, L, B). All confirm the transient scaling law (Equation 1).

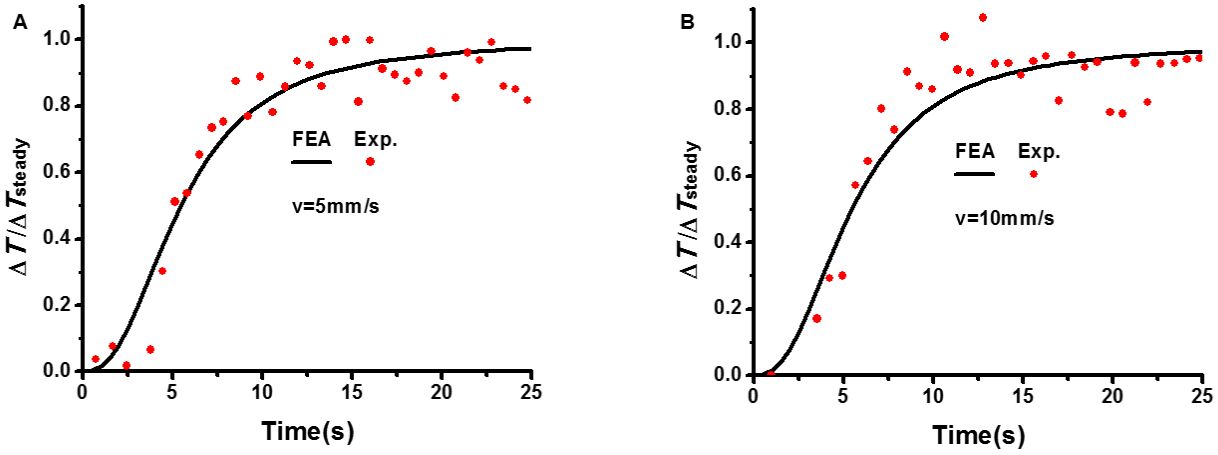

Fig. S4. Comparison between FEA and polydimethylsiloxane experiments. (**A**) The same conditions as Case 1 in Fig. S3, (**B**) double the flow velocity. The FEA agrees well with experiment without any parameter fitting. Experiments indeed show that the normalized temperature does not depend on the flow velocity.

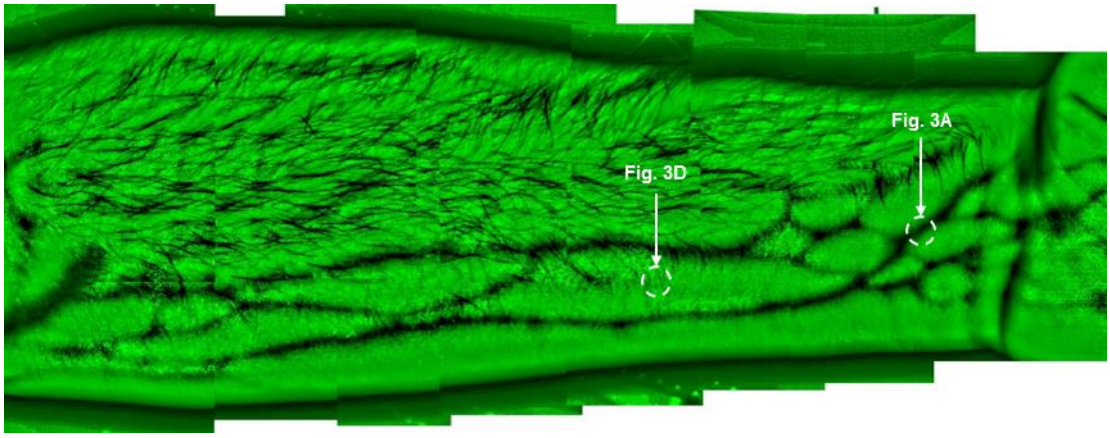

Fig. S5. Optical VeinViewer image used to accurately identify blood vessel locations. Labels indicator actuator placement during data collection for indicated figure.

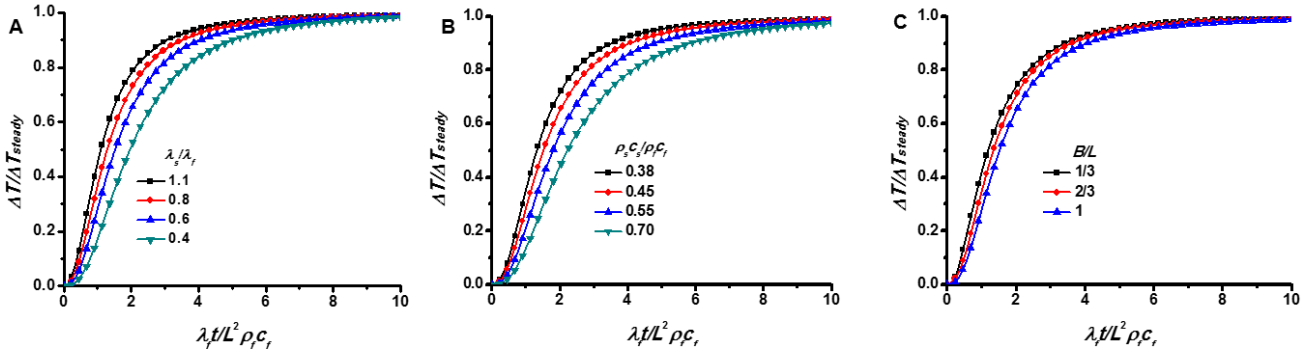

Fig. S6. The influence of variation of λ_s/λ_f, $\rho_f c_f/\rho_s c_s$, and *B/L* on the transient scaling law. The thermal parameters of the tissues (λ_s, ρ_s, and c_s) are highly variable, based on skin location, individual person, etc. We ran a clinical study of 25 people(*36*) in which we measured thermal diffusivities ($\lambda_s/\rho_s c_s$) that varied from 0.11 - 0.2mm^2s^{-1}, and thermal conductivities (λ_s) that varied from 0.2 - 0.55 $Wm^{-1}k^{-1}$. This corresponds to the parameters λ_s/λ_f=0.4 – 1.1, and $\rho_f c_f/\rho_s c_s$=0.38 - 0.7. (**A, B**) The transient scaling law (Equation. 1) with different λ_s/λ_f (*0.54 - 0.72*) and different $\rho_f c_f/\rho_s c_s$ (0.38 – 0.7), illustrates that the transient scaling law depends on the thermal parameters of the issues strongly. (**C**) The transient scaling law (Equation. 1) with B*/L=1/3 – 1*, shows the influence of the size of the actuator on the transient scaling law.

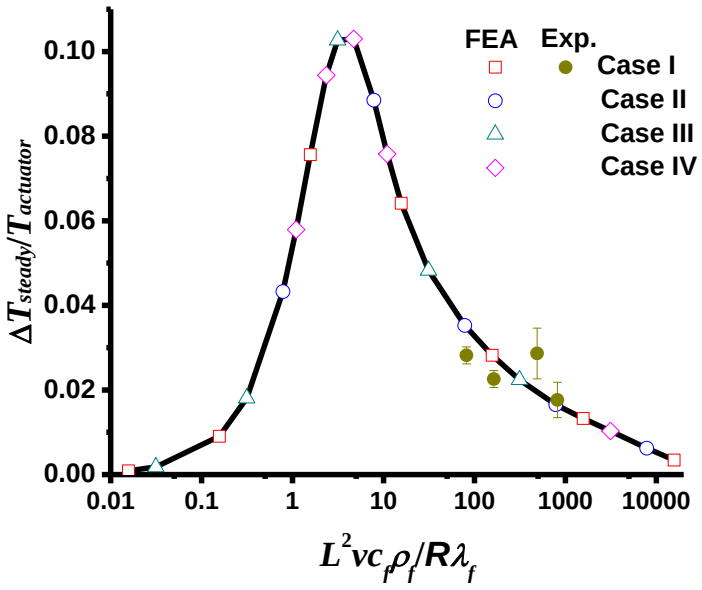

Fig. S7. Verification for the steady-state scaling law by FEA and experiments. Case I is the base line for comparison (water: λ_f=0.6W·mm^{-1}K^{-1}, ρ_f=1000kg/m^3, c_f=4184J·kg^{-1}·K^{-1}, PDMS: λ_s=0.18W·mm^{-1}K^{-1}, ρ_s=970kg/m^3, c_s=1380J·kg^{-1}·K^{-1}, h=0.55mm, L=1.5mm, B=1.5mm, R=1mm). Case II (double ρ_f) and Case III (double λ_f and λ_s) change the material properties while Case IV varies the geometric parameters (h, L, B, R). All confirm the steady-state scaling law. PDMS experiments agrees well with the steady-state scaling law without any parameter fitting.

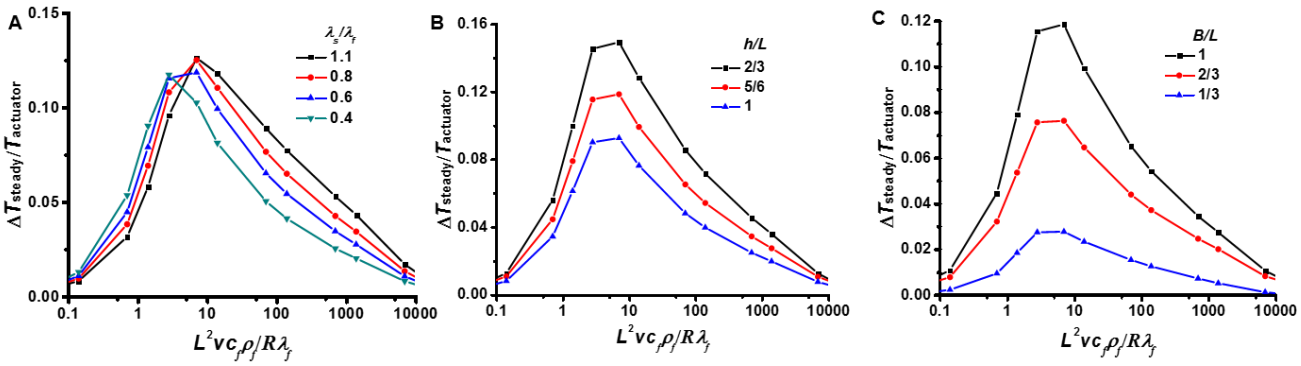

Fig. S8. The influence of variation of λ_s/λ_f, *h/L*, and *B/L* on the steady-state scaling law. The steady-state scaling law (Equation 2) with (**A**) different λ_s/λ_f (0.4 – 1.1), (**B**) different *h/L* (2/3 – 1) and (**C**) different *h/L* (1/3 – 1), illustrates that these three parameters all play an important role in the steady-state scaling law.

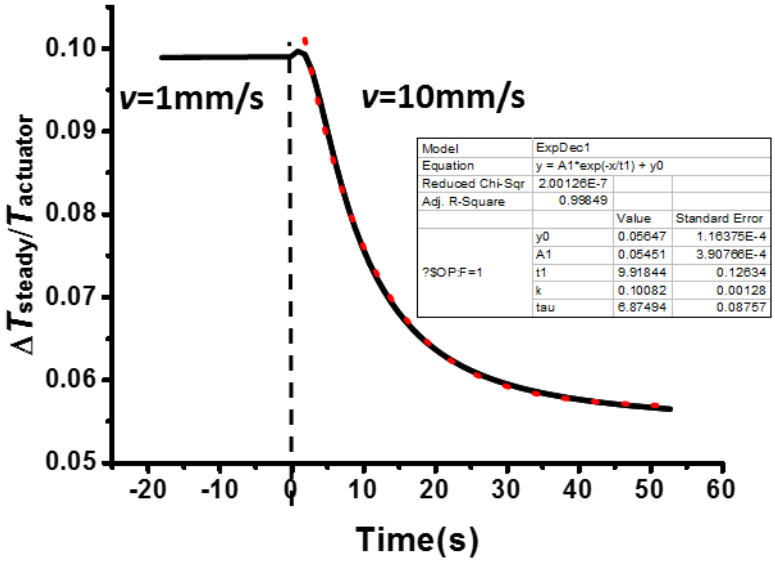

Fig. S9. Transient temperature response caused by flow speed change. All size and material parameters are the same as the case shown for R = 0.95 mm in Fig. 2E. A step-function increase in flow velocity (from 1 mm/s to 10 mm/s) results in a dimensionless temperature response as an exponential decay with a time constant of ~10 s. Conversely, a step-function flow decrease will result in a similar exponential growth function in sensor response.

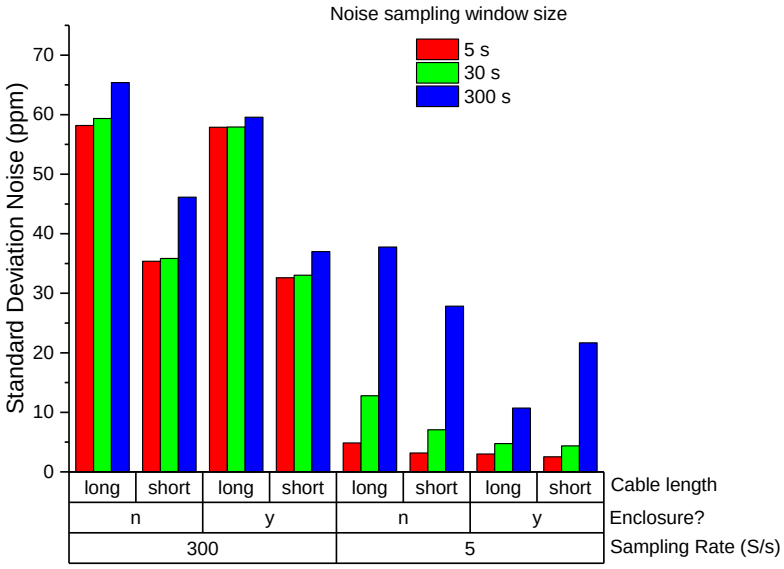

Fig. S10. Noise analysis of epidermal data acquisition system. Results from a series of benchtop experiments analyzing noise levels during different conditions. A change of 1 °C corresponds to a signal of 2500 ppm. At low sampling rates, and short sampling windows, a doubling of the data acquisition cable length results in a noise increase of 5% - 30%. Over longer sampling windows, noise increases significantly and is strongly influenced by placing the device in plastic enclosure from the ambient environment, indicating a dominance of environmental induced thermal changes. Over shorter sampling windows (5 s and 30 s), noise scales as (Sampling rate)$^{1/2}$. Over a 300 s sampling window, noise is dominated by environmental changes.

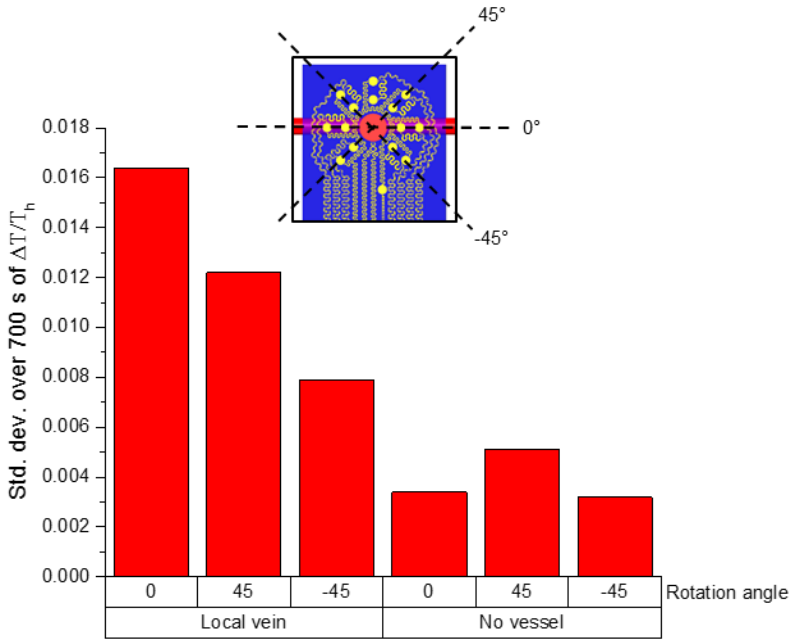

Fig. S11. Noise analysis of epidermal devices on skin. Results from a series of in vivo experiments analyzing noise levels when the device is placed over a vein, compared to a location with no significant visible veins. Results indicate the standard deviation of $\Delta T/ \Delta T_h$ over a 700 s sampling window. Analysis of different sensor pairing correspond to different rotation angles, where the rotation angle is the different between the measured sensor axis, and the vein axis. For the case of No vessel, the rotation angle simply corresponds to different sensor pairings. Signal variations are significantly lower in the case of no local vessel, and are maximized in the Local vein case of the sensor pair along the vein axis, which indicates that there is significantly more signal variation due change in flow through the vein.

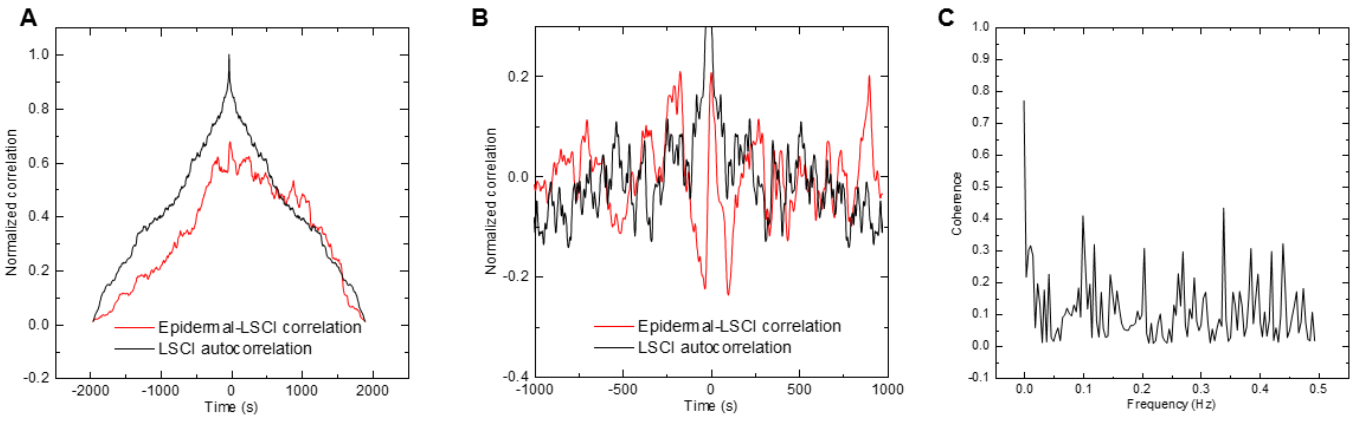

Fig. S12. Statistical correlation between LSCI data and epidermal device data from Fig. 4. LSCI autocorrelation shows the relative integral overlap area of the data when shifting the dataset relative to itself. For the autocorrelation, perfect correlation always occurs at t = 0, and the shape of the curve is determined by the time dynamics of the data. The autocorrelation represents a perfect correlation to the LSCI data. Epidermal-LSCI correlation shows the relative signal overlap area between the LSCI data and Epidermal device data, which closely matches that of the LSCI autocorrelation. (**A**) Correlation between raw data sets. (**B**) Correlation between linearly detrended data sets. (**C**) Coherence between linearly detrended datasets.

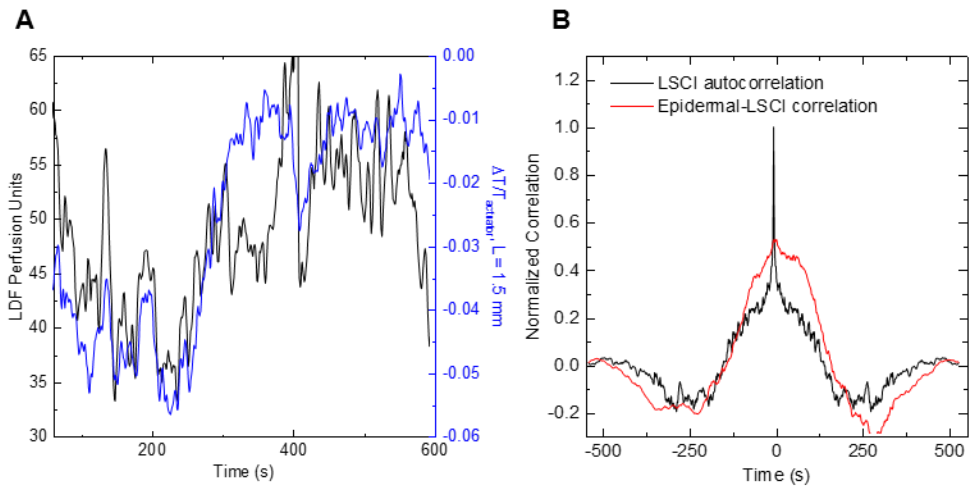

Fig. S13. Comparison between LDF signal and epidermal device signal during 10 min of natural flow on the volar aspect of the wrist of a male, age 33. (**A**) Laser Doppler and epidermal device signals. (**B**) Correlation between linearly detrended data sets.

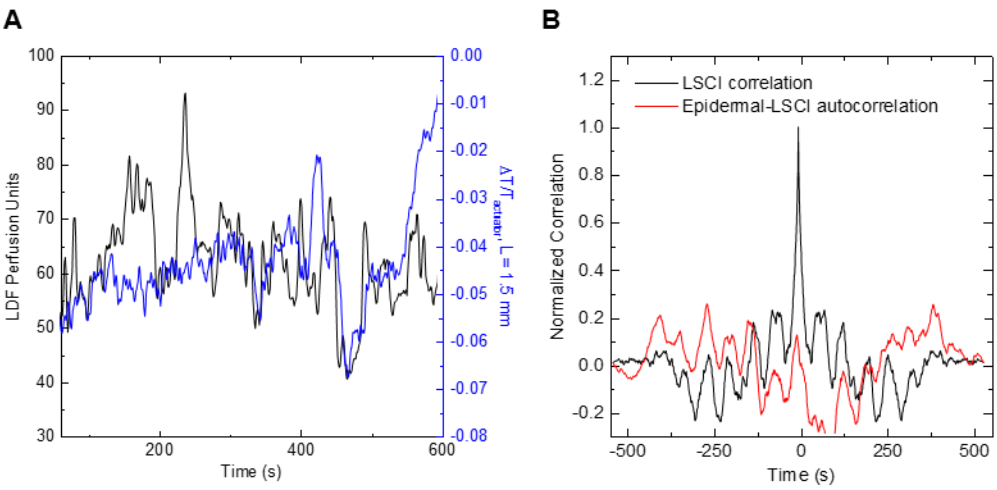

Fig. S14. Comparison between LDF signal and epidermal device signal during 10 min of natural flow on the dorsal aspect of the hand of a male, age 23. (**A**) Laser Doppler and epidermal device signals. (**B**) Correlation between linearly detrended data sets.

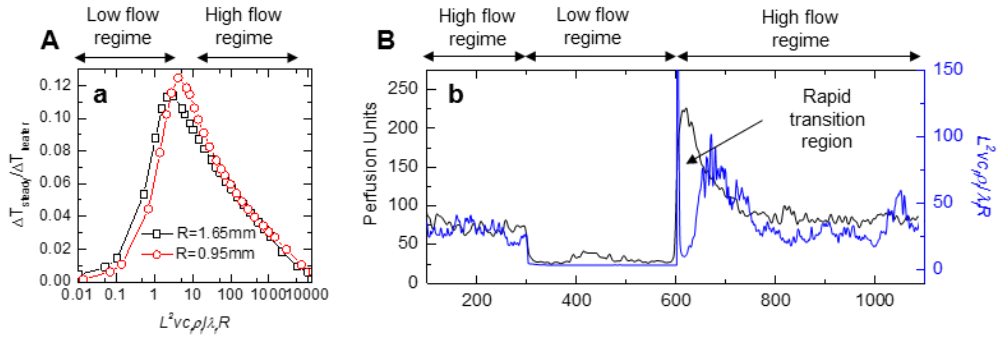

Fig. S15. Quantitative blood flow conversion of Fig. 5A. (**A**) Relation between thermal flow signals and blood flow rate, showing low flow and high flow regimes. When transitioning from very low flow to high flow, the relation between the thermal signal and blood flow changes sign, as well as functional form. (**B**) When the transition from low flow the high flow happens extremely rapidly, in a few seconds as in the experiment in figure 5a, the quantitative relation goes through a rapid transition from the low flow to the high flow regime. This results in a spurious signal depression in the rapid transition region, as indicated.

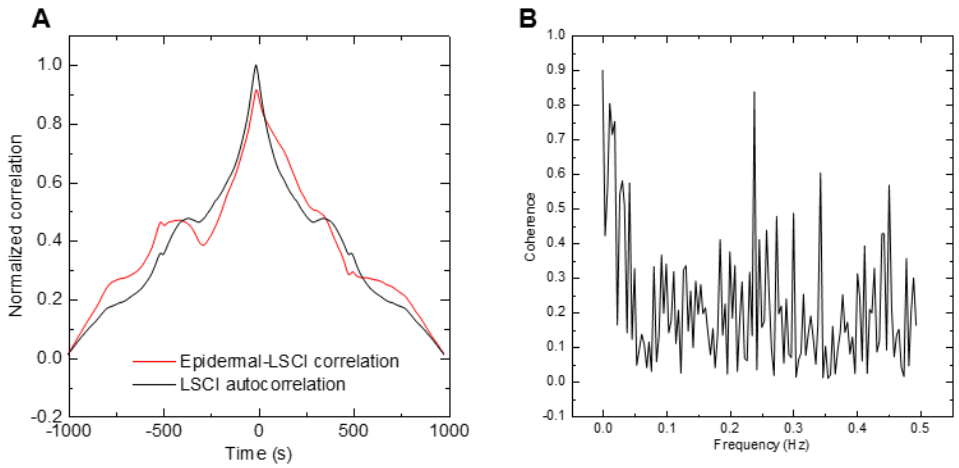

Fig. S16. Statistical correlation between LSCI data and epidermal device data from Fig. 5A. (**A**) Same analysis procedure at Fig. S10A. (**B**) Coherence between LSCI and epidermal device data.

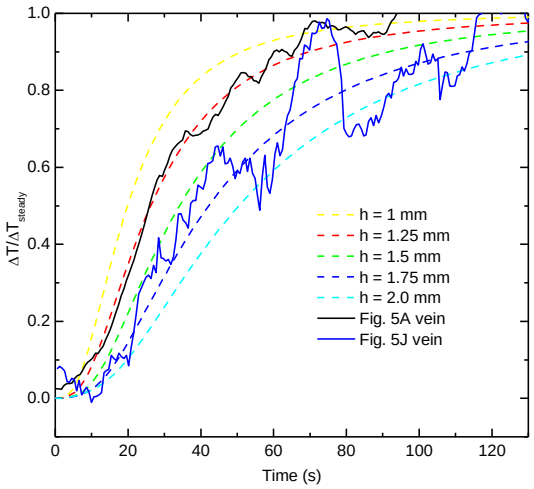

Fig. S17. Assessment of depth of vein associated with Fig. 5J. Same analysis procedure as described for Figure 2D. In this case, larger uncertainty in the measurement results from instability in the flow signal.

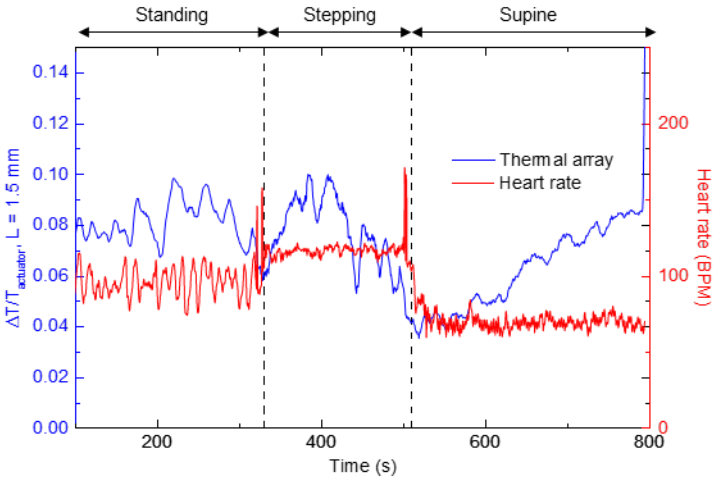

Figure S18. Device thermal signals during motion. The device is mounted above a vein on the wrist, as in other experiments. The subject begins by standing motionless for 5 minutes (30 s < t < 330 s). At t = 330 s, the subject begins a series of 48 steps up and over a 9 inch step that take place over a 3 minute period (Master's Step Test) until t = 510 s. The subject then quickly moves to a supine position (lying on the back) for the remainder of the experiment. No motion artifacts are apparent in the thermal data before, during, or after stepping. A pulse monitor is clipped to the finger to record heart rate data (relatively tolerant of motion due to the rigid clip), which confirms the period of stepping motion. We note that heart rate data is not equivalent to local blood flow measurements made by optical measurements in other experiments, and we do not attempt to make claims about specific flow correlations in this case, rather just demonstrate a lack of motion artifacts.

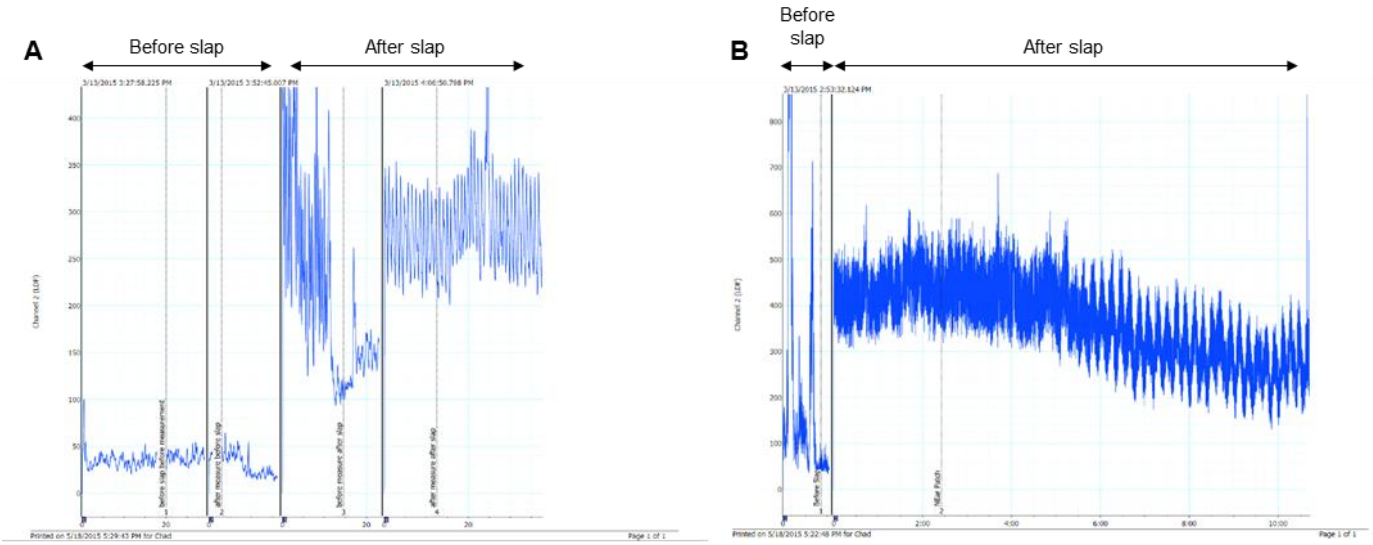

Figure S19. LDF measurements before and after slap-induced microvascular hyperemia. (**A**) LDF measurements corresponding to hyperemia shown in Fig. 6(A-D). (**B**) LDF measurements corresponding to hyperemia shown in Fig. 6(E-H).

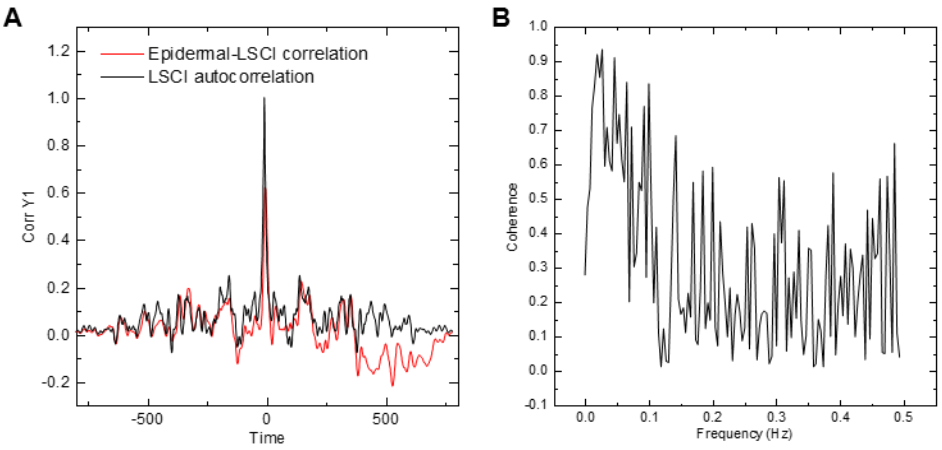

Fig. S20. Statistical correlation between LSCI data and epidermal device data from Fig. 7. (**A**) Same analysis procedure at Fig. S10B. (**B**) Coherence between LSCI and epidermal device data.

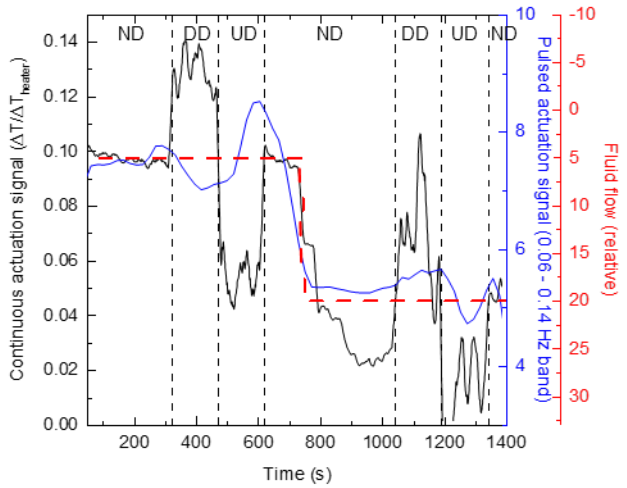

Fig. S21. Comparison of errors induced in the device response for continuous mode and pulsed mode actuation in a control experiment. The device is placed on a molded silicone flow system, designed to mimic a system with blood flow occurring beneath the surface of the skin in a large vessel. Thermal disturbances are applied to various sensors in the device array at various times during flow measurements. Disturbances are induced by bringing a hot solder iron tip, at 65 °C, in close proximity to the sensor either downstream (Downstream Disturbance, DD) or upstream (Upstream Disturbance, UD) of the actuator, without physically touching the sensor. The heat from iron the changes the relative temperature differential measured by the two sensors on opposing sides of the actuator, resulting in a measurement error. The experiment is carried out in continuous actuation mode (black; filtered with an adjacent averaging filter, window size = 20 points) and pulsed actuation mode (blue, 0.1 Hz actuation at 33% duty cycle; filtered with an adjacent averaging filter, window size = 4 points). Fluid flow begins at a baseline value of 5 and increases to 20 (relative values) at t = 740 s. The disturbance timing is as follows: 0 < t <320 s – No disturbance (ND); 320 < t < 470 s – DD; 470 < t < 620 s – UD; 620 s < t < 1040 s – ND; 1040 s < t < 1190 s – DD; 1190 < t < 1340 s – UD; 1340 s < t – ND. Induced errors occur in both the continuous and pulsed actuation modes, however the relative induced error in the pulsed actuation mode is ~20% that of the continuous mode.

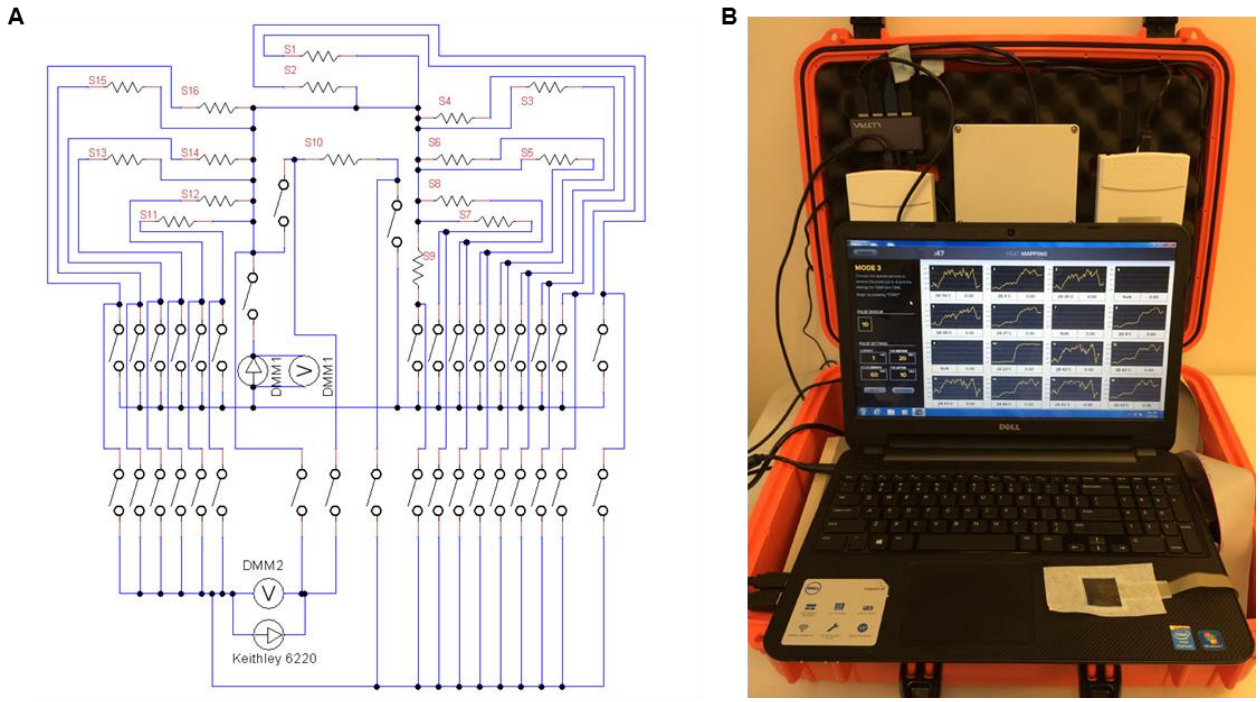

Fig. S22. Epidermal device (A) wiring diagram and (B) hardware setup. A detailed description of the system appears in the Materials and Methods section.

Movie S1A. Movie of LSCI and epidermal device signals over time for experiments presented in Fig. 3 (A to C).

Movie S1B. Infrared movie showing the sequential pressure applications for experiments presented in Fig. 3 (A to C) and movie S1A.

Movie S2. Movie of LSCI and epidermal device signals over time for experiments presented in Fig. 4 (A to D).

Movie S3. Movie of LSCI and epidermal device signals over time for experiments presented in Fig. 5 (A to I).

Movie S4. Infrared movie of thermal distribution over time due to device heating for experiments presented in Fig. 5 (J to M). Prominent pulsation near the actuator is seen during 400 s < t < 630 s, prior to reperfusion seen at t = 630 s. Movie speed is ~60x real-time. An arrow in the infrared movie shows the location of the pulses, which appear during the period of 460 s < t < 620 s. Text indicators also display during the movie to coincide with each pulse.